Analyst

PAPER

View Article Online
View Journal | View Issue

Cite this: *Analyst*, 2014, **139**, 6204

NMR–DMF: a modular nuclear magnetic resonance–digital microfluidics system for biological assays†

Ka-Meng Lei,[a] Pui-In Mak,*[a] Man-Kay Law[a] and Rui P. Martins[ab]

We present a modular nuclear magnetic resonance–digital microfluidics (NMR–DMF) system as a portable diagnostic platform for miniaturized biological assays. With increasing number of combinations between designed probes and a specific target, NMR has become an accurate and rapid assay tool, which is capable of detecting particular kinds of proteins, DNAs, bacteria and cells with a customized probe quantitatively. Traditional sample operation (*e.g.*, manipulation and mixing) relied heavily on human efforts. We herein propose a modular NMR–DMF system to allow the electronic automation of multi-step reaction-screening protocols. A figure-8 shaped coil is proposed to enlarge the usable inner space of a portable magnet by 4.16 times, generating a radio frequency (RF) excitation field in the planar direction. By electronically managing the electro-wetting-on-dielectric (EWOD) effects over an electrode array, preloaded droplets with the inclusion of biological constituents and targets can be programmed to mix and be guided to the detection site (3.5 × 3.5 mm^2) for high-sensitivity NMR screening (static B field: 0.46 T, RF field: 1.43 mT per ampere), with the result (voltage signal) displayed in real-time. To show the system's utility, automated real-time identification of 100 pM of avidin in a 14 μL droplet was achieved. The system shows promise as a robust and portable diagnostic device for a wide variety of biological analyses and screening applications.

Received 16th July 2014
Accepted 27th September 2014

DOI: 10.1039/c4an01285b

www.rsc.org/analyst

1. Introduction

Portable point-of-care (POC) diagnostic tools have become an attractive approach for global healthcare, especially for under-developed countries where advanced low-cost diagnostic tools are very limited.[1–6] In fact, for infectious diseases [*e.g.*, human immunodeficiency virus (HIV) and tuberculosis], any retardation in diagnosis can worsen the situations at both individual and community levels.[4,7]

A wide variety of point-of-care diagnosis tools have been available, such as the impedance and capacitance sensing,[8–10] both of which rely on a pair of electrodes (transducers) to quantify the biological/chemical targets between them. With pre-designed probes and magnetic beads, magnetic sensing is another way to detect the targets.[11,12] Bio-luminance detection is one more option to sense the amount of luminance emitted during the reaction of bioparticles such as pathogens and antigens.[13,14] Apart from these methods, nuclear magnetic resonance (NMR) is considered as a new tool for diagnosis.[15–17] Traditionally, NMR was used as an analytical tool for characterization of the structure of molecules and for chemical kinetics. Recent studies on NMR have successfully detected a number of biological targets, such as oligonucleotides,[15] proteins,[16,17] *Mycobacterium tuberculosis*[18] and bladder cancer cells, using a palm-sized permanent magnet.[19] In addition, with the advances in micro-electronics, NMR circuitry can be miniaturized in size while upholding adequate sensitivity suitable for a wide variety of biological assays. The underlying principle of NMR detection is to sense the NMR signal from the samples, which are mixed with target-specific magnetic-nanoparticles. The presence of the target in the samples will lower the spin–spin relaxation time (T_2), indicating the existence of the target rapidly in real-time.

One major challenge of micro-scale NMR is the operation of tiny samples beforehand, which can involve multi-step multi-site treatments. The samples under detection have to be mixed with the specific probes in one place and re-positioned to the sensing site inside the magnet for NMR. These procedures, regrettably, relied heavily on human efforts, degrading the throughput and consistency of diagnosis results while raising the chance of contamination. To address this issue, certain efforts have been undertaken to facilitate sample manipulation in NMR systems like capillary electrophoresis[20] and microfluidic channels.[17,21] Still, these methods involve several laboratory accessories (*e.g.*, pumps and pressure generators) and

[a]*State-Key Laboratory of Analog and Mixed-Signal VLSI and FST-ECE, University of Macau, China. E-mail: pimak@umac.mo*

[b]*Instituto Superior Técnico, University of Lisbon, Portugal*

† Electronic supplementary information (ESI) available: Electronics components of the system. Measured performances of the NMR sensing electronics. Received NMR signal of water from the system. See DOI: 10.1039/c4an01285b

fixed fluidic paths/pipes that have low portability and re-configurability.

In contrast, digital microfluidics (DMF) devices appear as a handy electronic-automated platform, allowing flexible droplet operations on a planar electrode array.[22–26] By exploiting the principle of electrowetting-on-dielectric (EWOD) to modify the surface tension, droplets can be guided and transported freely over the electrodes. Unlike the channel microfluidic devices, the routing paths of droplets in DMF can be customized and re-programmed by a computer program, opening up much design flexibility to manage droplets such as transporting, mixing and splitting. In addition, as the DMF chip is planar, all droplets can be preloaded on a chip before routinely executing the reaction or screening, enhancing the consistency of the experiments.

Here we describe the first lab-on-a-chip module unifying nuclear magnetic resonance and digital microfluidics (NMR–DMF) with simple electronics and a portable magnet, allowing non-invasive magnetic resonance diagnosis atop the DMF chip in real-time. One of the key challenges of integrating NMR on DMF is the geometrical limitation of the portable magnet. We managed to overcome this by introducing a figure-8 shaped coil such that the magnet can be placed parallel to the DMF chip and RF coil to better use the inner space of the magnet. To demonstrate that the system is capable of performing biological assays in a fully autonomous fashion, biotinylated magnetic nanoparticles were selected as the probe to detect the existence of avidin in the droplet samples. Results showed that the system can transport and mix the samples and probes over the DMF chip successfully. We anticipate that this portable NMR–DMF system will be broadly applicable to small-sample biological analyses.

2. NMR–DMF system prototype

Fig. 1(a) shows the overview of the NMR–DMF system. It was designed to drive the droplets under detection and target-specific probes, if any, to the desired location for NMR assays. The movement of droplets is handled by an electrode array, which was fabricated on the glass substrate. The RF-coil functions as a transducer transforming the magnetic field to voltage (or *vice versa*). The electronics transmit the excitation signal to the RF-coil and receive the NMR signal from it. The results are collected by an oscilloscope in this prototype (for portability, by an analog-to-digital converter to interface with the computer). The relaxation times are derived by a software algorithm. The DMF platform and NMR coils are customized in size to befit the limited inner volume of the magnet; moreover, the design considerations of the system are introduced as follows.

Nuclear magnetic resonance

Magnet. The portable permanent magnet is responsible for magnetizing the nuclei of the atoms. Atoms like ^{1}H, ^{2}H, ^{13}C and ^{19}F can be analysed, but due to the natural abundance, stability and commonness of hydrogen atoms (in water), this design focuses only on the hydrogen atoms.[27] The strength of the magnet correlates to the Larmor frequency and the signal-to-noise-ratio (SNR) of the sensed output:[28]

$$\omega_{\mathrm{L}} = \frac{f_{\mathrm{L}}}{2\pi} = \gamma B_0 \tag{1}$$

$$\Psi_{\mathrm{rms}} \propto KB_1 \sqrt{\left(\frac{1}{Fl\xi\Delta f}\right)} \frac{{\omega_{\mathrm{L}}}^{7/4}}{\sqrt[4]{\rho}} \tag{2}$$

with gyromagnetic ratio γ, permanent magnet field strength B_0, homogeneity factor K, magnetic field strength per unit current produced by the RF-coil orthogonal to the permanent magnetic field B_1, noise figure of the receiver's forefront amplifier F, length of the RF-coil conductor l, bandwidth of the system Δf and resistivity ρ of the RF-coil. From eqn (1) and (2), the SNR of the system is proportional to the power of 7/4 of the magnetic field strength B_0. Although there seem to be numerous ways to enhance the magnetic field (*i.e.*, for higher resolution and lower noise), the portability and power consumption of the system will be penalized due to the need for a heavier and bulkier magnet, not to mention a higher operating frequency that will be required for the electronics.

To balance the system performance with its portability, a 0.5 T permanent magnet was chosen. It is 1.25 kg in weight and 1005 cm^3 in volume. The corresponding f_{L} of the hydrogen atom under this magnet strength is ~21 MHz.

Electronics and back-end signal processing. The electronics of the NMR–DMF system were mainly built by discrete components for fast prototyping and greater flexibility to integrate with the DMF electronics.

The schematic of the electronics is depicted in Fig. 1(b), which mainly consists of two paths: transmitter and receiver. Before the nuclear spins can induce signal to the coil, they have to be excited by the coil at f_{L}. Since the Carr–Purcell–Meiboom–Gill (CPMG) sequence is applied, both in-phase (I) and quadrature (Q) waveforms are collected. By applying frequency division, a pair of equal-pulse-width I and Q signals can be generated under a clock-signal frequency 4 times that of the Larmor frequency. To prevent the SNR of the system from degrading by the flicker noise of the electronics, the clock frequency was chosen at $4(f_{\mathrm{L}} + f_{\mathrm{IF}})$. Although the excitation frequency is shifted to $f_{\mathrm{L}} + f_{\mathrm{IF}}$ instead of f_{L}, the atoms can still be excited if f_{IF} is small enough, which also facilitates the design of the electronics.[19] Since the RF-coil serves both the transmitter and receiver, switches have to be used to isolate the excitation signal from leaking to the receiver. For the transmitter, output buffers were utilized to boost up the driving capability. The operating phases of the switches and buffers are controlled by a field-programmable gate array (FPGA).

The receiver can amplify the weak signal coupling from the RF-coils. The weak amplitude of the induced NMR signal is at a level of 100 nV to 40 μV.[29] The first amplification is based on an LC tank to provide a passive gain Q to the signal, where Q is the quality factor of the RF-coil.[19,29,30] The noise figure of the receiver will then be suppressed by Q, and the overall SNR will be increased according to eqn (2). The input impedance of the forefront amplifier should be adequately large to prevent its

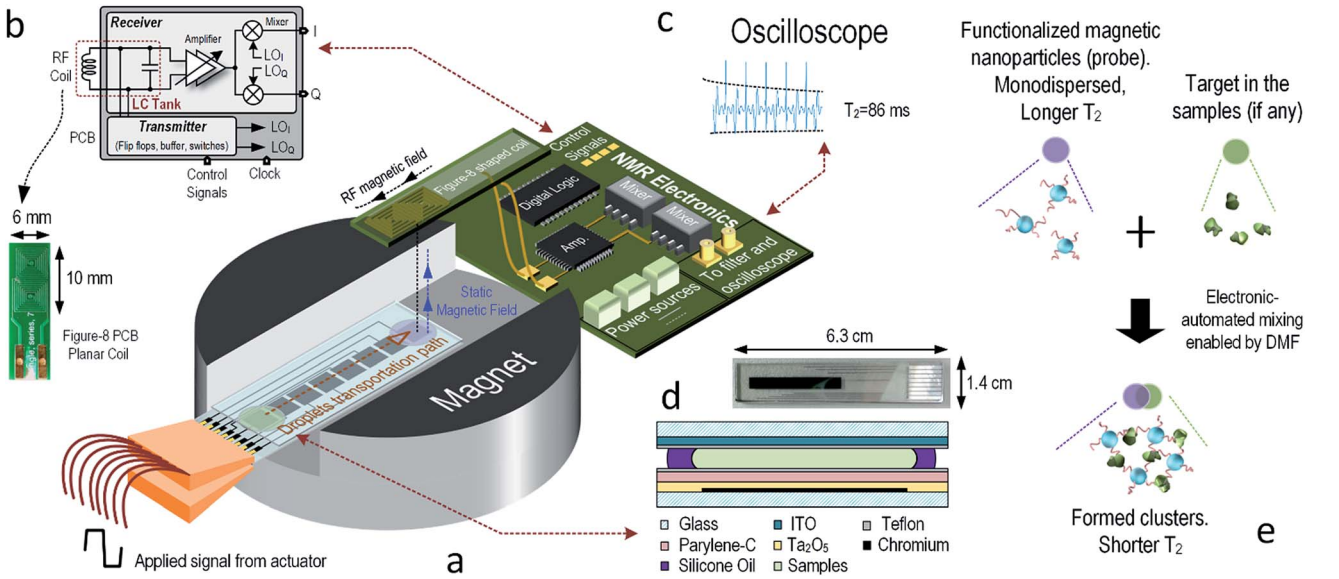

Fig. 1 The overall schematics and operations of the NMR–DMF system. (a) The placement of the DMF chip, magnet, RF coil and PCB board in 3D view. Because of the plane-parallel magnetic field generated by the figure-8 shaped coil, the NMR system can be effectively integrate into the DMF system; (b) schematics of the NMR Electronics. The transmitter which is formed by the digital logics such as flip flops, is used to excite the hydrogen atom. On the receiver part, the capacitor together with the RF-coil (fabricated figure-8 shaped coil) forms an LC tank to provide passive gain enhancing of the system's sensitivity. The signal is then amplified and down converted to f_{IF} (intermediate frequency) and fed to the external filters and oscilloscope; (c) the filtered results from the PCB are captured by the oscilloscope for easier demonstration purpose. Waveforms are then analysed and the spin–spin relaxation time (T_2) is fitted by the algorithm written in MATLAB; (d) the photograph of the DMF chip and structure of the DMF platform. The droplets are squeezed between the top and bottom planes and surrounded by silicone oil; (e) the detection mechanism of the NMR–DMF system. The target-specific magnetic nanoparticles, which act as probes, are placed on the sensing site initially (in purple). The samples at other electrodes (in cyan) will be transported to the sensing site and mixed with the probes to perform NMR assays automatically by applying voltage on corresponding electrodes. Without the target, the probes stay monodispersed and will have a longer T_2. Otherwise, the target and probes will form clusters by forming bonds between each other, and the T_2 will be decreased.

loading effects from the LC tank, which otherwise deteriorate the sensitivity. Obviously, the noise performance of the amplifier is decisive to the SNR of the receiver. In addition, as the signal amplitude is not consistent because of the uncertainties of the sample volume and biological constituents inside the samples, variable-gain amplifier is necessary for compensation.

After signal amplification, the signal is driven to the I and Q mixers for down-conversion to f_{IF}, which also allows filtering of the high-frequency noise superimposed into the signal. Passive mixers befit this system as they generate less noise than its active counterpart. The resulting signals are then low-pass filtered and further amplified before driving into a digital oscilloscope [Fig. 1(c)] to reduce the uncertainty due to quantization error. According to eqn (2), the bandwidth of the filter should be set carefully to prevent excessive out-of-band noise. Finally the signals are collected for back-end processing such as I/Q demodulation and T_2 derivation. The echoes' amplitude decays exponentially, and an algorithm written in MATLAB was built to derive and fit to this exponential curve:

$$A_{\text{peak}}(t) = A_{\text{o}} e^{-\frac{t}{T_2}} \quad (3)$$

where $A_{\text{peak}}(t)$ is the amplitude of the echo at the time t, and A_{o} is the original amplitude of the echo. By substituting different pairs of values of $A_{\text{peak}}(t)$ and t, the values of A_{o} and T_2 are derived.

RF coils. The RF-coils are the interface between the droplet samples and electronics. They transduce the magnetic field produced by the hydrogen atoms to the voltage for the receiver. There are different kinds of coils such as saddle shaped coil,[28] solenoid[19,28,29] and planar coil.[19,30] The saddle shaped coil and solenoid either required hand-wrapping or extra fabrication process. In fact, the planar coil (this work) on a low-cost, two-side printed circuit board (PCB) is appealing for its consistency of parameters and disposability under volume production.

Typically, the planar coil is a circular spiral as shown in Fig. 2(a). The dominant magnetic field of this kind of RF-coil is in its axial direction. This spiral coil is common due to its high sensitivity, but the magnetic field from the RF-coil has to be orthogonal to the static magnetic field from the magnet, posing a physical limitation on the position of the coil. Illustrated in Fig. 2(b), the PCB coil has to be within the gap (12 mm) of the magnet, limiting the number of electrodes that can be integrated. One way to surmount this obstacle is to use a single-sided magnet with a surface-parallel magnetic field,[31] where static and RF magnetic fields will be orthogonal to each other. However, this kind of magnet has to be customized, and the magnetic field is weaker when compared with the chosen (0.2–0.5 T). In fact, as another dimension of the gap is 50 mm in length, we make use of a figure-8 shaped coil to resolve this issue as shown in Fig. 2(c).[32–34] Here, a square coil

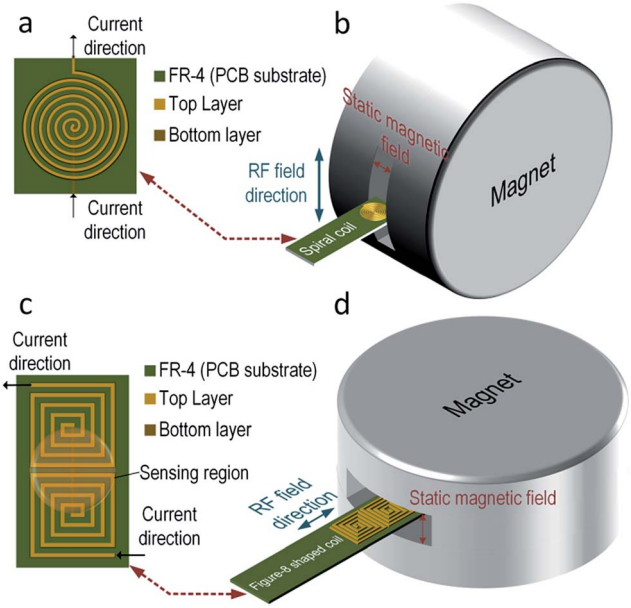

Fig. 2 (a) Illustration of a conventional spiral coil; the magnetic field generated by the current as shown in the figure will have the out-of-paper direction. The shape of the coil is typically circular to enhance the magnetic field at the center; (b) the placement of the magnet and the conventional spiral coil. Due to the fact that RF-field from the coil and magnetic field from the magnet have to be orthogonal to each other, the spiral coil and magnet must be configured as shown in the figure, which is not suitable for the DMF platform. (c) Illustration of the figure-8 shaped coil. Generally, it is composed of two spiral coils in reversed direction (CW and ACW) in series, and the field between two coils generated by the current shown in the figure will have a direction pointing downward, and it is the sensing region in our system. The shape of a single coil is square instead of circular to enhance the magnetic field at the sensitive region; (d) placement of the magnet and the figure-8 shaped coil. Since the magnetic field goes parallel to the PCB substrate direction, the magnet and the coil now can be placed as shown in the figure, and the DMF platform can be effectively integrated with the NMR.

is utilized instead to enhance the magnetic field at the boundary. The figure-8 shape indicates that there are two coils with opposite axial magnetic field direction placed next to each other and connected in series. In this way, the magnetic field coupled between the centers of the two coils will be in-phase and constructively summed, as it is an effective sensing region of the coil.

With the same number of turns per spiral, the figure-8 shaped coil induces more thermal noise than the spiral coil since the length of the conductors is doubled. According to eqn (2), the SNR will be increased accordingly. However, it has been proven that the figure-8 shaped coil is less susceptible to environmental couplings (*e.g.*, powerline cables, equipments and RF interference) since they appear as a common-mode noise.[35–37] In addition, as depicted in Fig. 2(d), the RF-field direction of the sensitive region is parallel to the PCB. This indicates that the PCB-coil can be located horizontally with the gap of the magnet, enlarging the space 4.16 times for the DMF chip.

Digital microfluidics

DMF platform. DMF is a lab-on-a-chip technology based on the principle of electrowetting-on-dielectric (EWOD). Droplets are manipulated *via* surface-tension modulation induced by an electric field, enabling electronic-automated chemical/biological reactions with low sample volumes. Differing from the conventional microfluidics, the metallic electrodes, dynamic actuation signal and discrete droplet controllability constitute a highly efficient droplet-management POC platform for disease diagnostics.[22–26] The principle of DMF is to change the contact angle between the droplets and substrate by electric fields. When there is no electric field applied to the electrode under the Teflon layer, the surface of the Teflon is hydrophobic. However, when the electric field is present, the surface will become hydrophilic. As a result, the droplets can be manipulated easily by voltage signals.

The structure of a DMF platform is shown in Fig. 1(d), and it is composed by an electrode array. The electrodes are formed by chromium. ITO (Indium Tin Oxide) acts as a ground plane for the electric fields and is coated on a glass substrate. To integrate the NMR and DMF, the DMF chip is sized for inserting into the magnet for magnetizing the samples, and the coil is located over the samples for high-sensitivity sensing.

However, as the electrode (chromium) and ITO are made by conducting materials, the Q of the coil will be degraded when they are placed near the coils, due to the eddy currents formed in the conductors. The energy loss per cycle in the conductors by eddy currents (when the skin effect does not take place) is given as follows:[38]

$$W_{\text{loss}} = \frac{(\pi \cdot B_{\text{RF}} \cdot d \cdot f)^2}{6\rho} \cdot (A \cdot d) \quad (4)$$

with magnetic field generated by the RF-coil on the conductor B_{RF}, thickness of the conductor d, cross-section area of the conductor A, frequency of the magnetic field f and the resistivity of the conductor ρ. By the law of energy conservation, the energy losses in the conductors are generated from the RF-coil, causing Q degradation of the coil. To maintain Q of the coil, the eddy current loss in the nearby conductor must be minimized. The eddy current loss in chromium is negligible in most cases, as it has sheet resistance >100 Ω sq^{-1}. However, for ITO, its sheet resistance can vary from 5 to 500 Ω sq^{-1}. ITO with higher sheet resistance may lead to slower droplet motion, but it will decrease the eddy current loss. Moreover, the SNR of the NMR signal will be reduced with diminishing B_1 according to eqn (2), and the eddy current generated by the conductor will diminish the effective B_1. From eqn (4), the thickness of the ITO should be optimized to reduce the eddy current loss as it will rise proportionally to the cube of d. Moreover, to ensure the droplet movement and reduce the required driving voltage, silicone oil was injected to fill the gap between the ITO layer (top plate) and DMF chip (bottom plate).

Electrodes actuator. The driving signal of each electrode is a 50%-duty-cycle square wave. To avoid the overstress conditions, the driving signals are clipped by diode protection scheme. To move a droplet to the desired electrode, the driving signal will

be connected to the correlated pads while the neighbouring electrode was grounded to prevent excess charges stored in the electrodes that otherwise might cause dielectric breakdown.

3. Materials and methods

Permanent magnets

Magnets PM-1055 was purchased from Metrolab (Switzerland). It has a nominal magnetic field of 0.5 T. The actual magnetic field was confirmed by Tesla Meter DTM-150 with probe LPT-130 from Group 3 Technology Ltd. (New Zealand) before the NMR experiment took place to ensure the applying frequency matches with f_L given in eqn (1). In addition, since the magnet has a temperature coefficient of -1200 ppm K^{-1}, the temperature of the testing environment has to be tracked to ensure the excitation frequency is not shifted from f_L after temperature variation. This process was performed by a digital thermometer from Agilent (Santa Clara, CA).

Electronics

The electronics detailed in ESI† was mounted onto a low-cost PCB. The control parts are linked to FPGA DE2 from Altera (San Jose, CA). The resulting signal from the PCB was filtered by the low-pass filter SR640 from Stanford Research Systems (Sunnyvale, CA). It filters out the high-frequency noise and offers extra signal gain. Finally, the signal was displayed on a digital oscilloscope DSO91304A from Agilent. To measure the overall signal gain, a sinusoidal test signal generated from signal generator E4436B, Agilent is injected into the receiver. The signal coming out from the low-pass filter is connected to a signal analyzer N9030A from Agilent.

RF coils

The coil's layouts were drawn *via* Altium Designer Summer 09 (Australia). The turn spacing and width of the conductor in the coils are both 0.15 mm. The leads of the coils were drawn wide enough to minimize the loss. The thickness of copper in the PCB is ~26 μm. The received coils were characterized by an impedance analyzer 4294A from Agilent. Four samples were measured for each type of coil to demonstrate the reproducibility. The performance and characteristics of the coil are studied by COMSOL™. The strength and direction of the magnetic fields are simulated by injecting a current of 1 A through the coil.

Signal post-processing

The signals displayed on the oscilloscope were collected and analyzed by MATLAB (Natick, MA). The peak echo of the signals was detected and fit into the regression model to derive the T_2 of the echo trains.

Samples

De-ionized water was firstly tested to ensure the functionality of the system. Then, different concentrations of copper sulfate ($CuSO_4$) diluted from $CuSO_4 \cdot 5H_2O$ were tested. Bio-assays were performed to ensure the practicability of the system. The bio-samples in this experiment were biotinylated iron nanoparticles and avidin from MicroMod (Germany). The size of the nanoparticles is 100 nm and the concentration of iron nanoparticles is 0.2 mM; moreover, the concentration of avidin is 1 mg mL^{-1}.

NMR settings

The sample volume for the NMR testing alone is 5 μL. The $\pi/2$ pulse widths for the coil was first estimated by calculation and then calibrated by observing the amplitude of the free induction decay of the NMR signals. Spacing between the echoes was set to 10 ms for the water and $CuSO_4$ sample and 3 ms for magnetic particles. 30 echoes were collected for each NMR measurement, and each measurement was repeated 16 times to enhance the signal SNR. After each measurement, the system halted for 5 s before the next experiment to ensure that the atoms stop vibration and they have been magnetized stably by the magnet.

Digital microfluidics chip

The ITO glasses were purchased from Huanan Technology Ltd. (China). Thickness of the overall glass is 0.5 mm. The pattern of the electrode was drawn in AutoCad (San Rafael, CA). The process of fabrication of the DMF platform is similar to the one stated before.[25] The volume of liquid under testing per electrode (without mixing) is 7 μL. The electrodes were driven by a square wave with a peak-to-peak voltage of 40 V and a frequency of 1 kHz. The size of the electrodes is 3.5×3.5 mm^2, and the gap between the top and bottom planes is 0.45 mm.

4. Experiment and results

Magnets

To approximately locate the Larmor frequency of the hydrogen atoms, the magnet's field strength was first measured. The magnetic field at the center of the magnet is around 0.4615 T at 20 °C, which corresponds to a f_L of 19.65 MHz.

RF coils

Several figure-8 shaped coils were optimized in COMSOL with a three-dimensional model before fabrication to determine the required number of turns. The fabricated coils were measured with an impedance analyzer and compared with the simulations to confirm the parameters. Table 1 shows two sets of parameters for the coil with 14 and 18 turns. The difference between the simulation and measurement results is sufficiently small (<7%). Such error could be originated from the leads of the coils in the measurements, coarse meshing in 3-dimensional simulation and the thickness variation of PCB copper traces. Nonetheless, the accuracy is adequate here as only the trend and magnetic field direction are decisive. This also offers a systematic study of the RF-coils when compared to the solenoid and saddle-shaped coils. Another advantage of the PCB coils is the reproducibility. From Table 1, the reproducibility of the PCB coils was adequately high as the standard deviations are <3% of the nominal values. This feature makes PCB coils attractive, as the fabrication only relies on machines, minimizing the variation between the same style of

Table 1 Summary of the measured and simulated figure-8 shaped coil parameters at 20 MHz. For measurement data, 4 coils are measured for each case, with mean-value together with standard-deviation shown. The results show that the coils have high accuracy (<7%) and reproducibility (<3%). Sims: simulation; Meas: measurement. Parameters: copper thickness = 26 μm, FR-4 relative permittivity = 4.5

Turns	Resistance	Inductance	Quality factor
14 (Sim.)	1.44 Ω	347.80 nH	30.29
14 (Meas.)	1.52 ± 0.04 Ω	373.4 ± 2.7 nH	31.0 ± 0.6
18 (Sim.)	2.39 Ω	646.58 nH	34.01
18 (Meas.)	2.48 ± 0.03 Ω	687.0 ± 4.4 nH	34.8 ± 0.3

coils. The magnetic field strengths of figure-8 shaped coils *versus* vertical distance were simulated in Fig. 3(a). The magnetic field decays along the *z*-axis as expected. Thus, to maximize the sensitivity, the samples under test should be close to the coil's surface according to eqn (2). The unit magnetic field strength is 1.8 mT adequate for our system.

Commercial tesla meter (*e.g.*, DTM-150) can only measure AC magnetic field up to 3 kHz. Thus, only simulation results are presented to demonstrate the magnetic field direction of the figure-8 shaped coil under unit current injection. The magnetic-field profile of the 14-turn coil is plotted in Fig. 3(b), where the magnetic flux lines between the two coils align with the *y*-direction (*i.e.*, parallel to the PCB surface).

Electronics

The measured gain of the mixer is 95.7 dB within 5 kHz of IF for the receiver. The output signal of the system with a 100 nV sinusoidal input is 30 dB above the noise floor, and thus it can detect a signal amplitude down to 100 nV. Data about the electronics measurement can be found in the ESI text and Fig. S1 and S2.†

NMR systems

The pulse width of the figure-8 shaped coil was determined by varying the RF excitation pulse duration and observing the

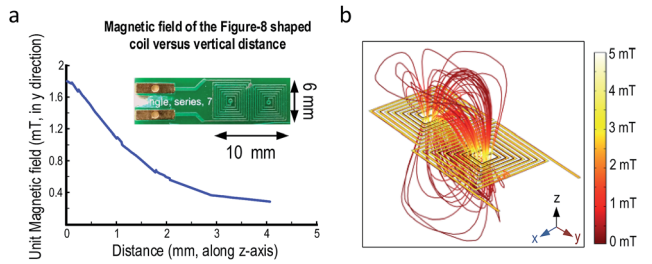

Fig. 3 (a) Plot of unit magnetic field in *y*-direction of the 14-turn figure-8 shaped coil along *z*-axis. The magnetic field is stronger on the coil surface (1.8 mT) and starts to decrease above the coil. Inset shows the photograph of the 14-turn figure-8 shaped coil; (b) the magnetic flux lines of the simulated 14-turn figure-8 shaped coil. The magnetic fluxes are still pointing in the *z*-direction at the centres of each coil. However, between the two coils, the magnetic flux is pointing in the *y*-direction, generating plane-parallel magnetic flux.

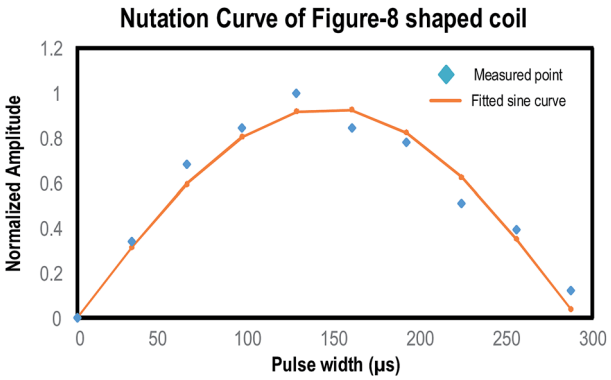

Fig. 4 Nutation curve of the 14-turn figure-8 shaped coil. The normalized amplitude from different durations of RF excitation signals was recorded and fitted to the sinusoidal wave. The estimated π/2 pulse widths for the coil is 144 μs.

corresponding NMR signal. Fig. 4 shows the plot of such a nutation curve. The π/2 pulse for the 14-turn figure-8 shaped coil is estimated as 144 μs.

Before integration of the NMR–DMF system, the NMR part was tested separately to verify its own functionality. According to the study, $CuSO_4$ will affect the T_2 of water.[39,40] $CuSO_4$ with different concentrations was prepared for the experiment. A 14-turn figure-8 shaped coil was selected for the NMR system.

Fig. 5(a) shows the received NMR signal of water from the figure-8 shaped coil. T_2 derived by the algorithm is 343.6 ms. The glitches appearing between the echoes correspond to the excitation signal. They can be prevented by adding switches at the receiver front-end. Yet, since this will contribute with noise to the signal, they are left together with the echoes. Nevertheless, it will not affect the derivation of T_2 since the algorithm will ignore the excitation signal. Moreover, the amplitude of the first echo is smaller when compared to the second and third echoes. This is caused by the superposition of different coherence pathways.[41,42] Since the first echo is severely interrupted by this effect, leading to an amplitude smaller than expected, it will be excluded from the curve fitting algorithm to exclude the error.

The relation between the concentrations of $CuSO_4$ and T_2 was depicted in Fig. 5(b). $1/T_2$ is increased linearly with the concentration of $CuSO_4$ (0.9866 mM^{-1} s^{-1}).

Digital microfluidics chip

The thickness of the coated ITO can be determined by eqn (4). The magnetic energy generated from the 14-turn figure-8 shaped coil unit current is 144 nW. In order to preserve the quality factor of the coil, the thickness of the ITO coating should be evaluated. Fig. 6 shows the eddy current loss on the ITO generated by a unit current passing through the 14-turn figure-8 shaped coil against the ITO thickness. The eddy current loss should be diminished by less than 0.5% of the magnetic energy generated by the coil, which was marked on Fig. 6. The thickness is limited to 80 nm, which is equivalent to a sheet resistance of 12.5 Ω sq^{-1}. ITO with sheet resistance of 100 Ω sq^{-1} was chosen for the system.

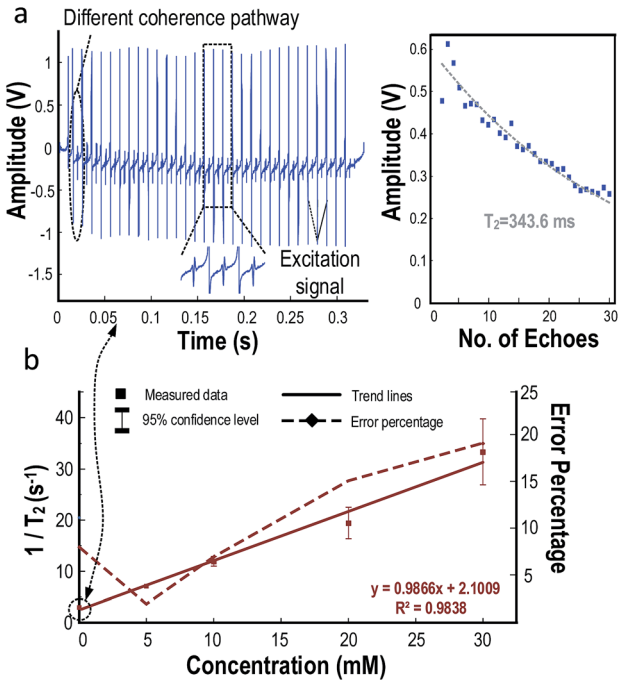

Fig. 5 (a) Received NMR signal from water. The received signal is composed of trains of echoes induced by the CPMG pulses. The glitches between the echoes are the excitation pulses. Usually, the first echo is neglected for relaxation time derivation since it is interfered by a different coherence pathway. Inset shows the enlarged received NMR signal. The echoes are clear, and their peak-to-peak amplitudes were plotted on the right axis against time, with a decreasing exponential manner, which was bounded by the grey dotted trend line. The derived relaxation time by the algorithm in this case is 343.6 ms. (b) Transverse relaxation time of the NMR signal *versus* concentration of $CuSO_4$ solution, and results were shown on the graph (■). The trend lines were drawn together with their equation and R^2 value. 95% confidence levels were marked on the graph (—). In addition, the error percentages (defined as half of 95% confidence level/true value) are marked on the graph with dot lines where the values were displayed on the right axis *i*.

Fig. 7(a) shows the fabricated DMF chip. It consists of only 8 electrodes in a row for this prototype, and thus only one assay can be performed each time. Yet, this system can still demonstrate the idea of integrating NMR assays with the DMF platform. Fig. 7(b) and (c) show the original and final positions of the droplet. The droplet was transported from electrode no. 1 to no. 8, which is the NMR sensing site, by applying a signal on the electrode properly. The velocity of the droplets is ~1.8 mm s^{-1}. No obvious distinction of droplet movement was observed with and without a strong magnetic field, as expected, since the DMF works with the electric field for droplet manipulation.

Nuclear magnetic resonance on digital microfluidics chip

The proposed system integrates two core technologies: NMR and DMF. Integration with the DMF system can enable NMR to be performed in a more automatic and controllable way. Related image of the prototype and detailed testing result from water can be found in the ESI (Fig. S3†).

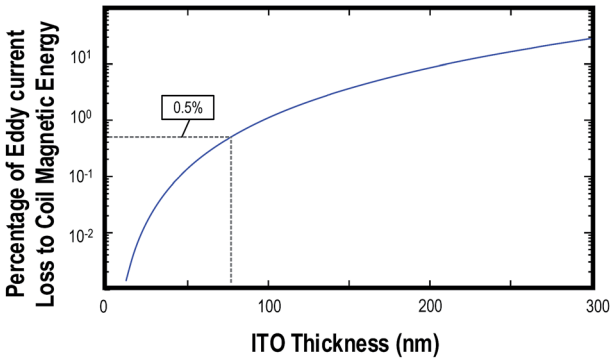

Fig. 6 Percentage of Eddy current loss generated by the 14-turn figure-8 shaped coil to coil magnetic energy against the thickness of the ITO glass. The figure was plotted based on (4) with $f = 20$ MHz, $\rho = 1 \times 10^{-6}$ Ωm, $A = 40$ mm × 24 mm, which is 4 times the dimension of the figure-8 shaped coil. B_{RF} is the magnetic field on the ITO. For accurate prediction, B_{RF} should vary according to the relative position of the ITO compared to the coil. Here, only the peak magnetic field at the position of ITO (which is 1.5 mT from Fig. 3) is substituted. The dotted line shows 0.5% level and corresponds to the ITO thickness of 80 nm fr.

For biological assays, the NMR–DMF system was operated to test the presence of avidin in the water sample using biotinylated magnetic nanoparticles as a probe.[17,19] When avidin is absent from the samples, the biotinylated nanoparticles will stay monodispersed. Yet, if avidin exists, avidin and biotin will form rigid bonding, and the nanoparticles will aggregate and form large clusters. These clusters will perturb the neighbouring magnetic field and concomitantly decrease the T_2 of the protons (*i.e.* decay faster), and thus the NMR system can detect the existence of avidin in real time. The

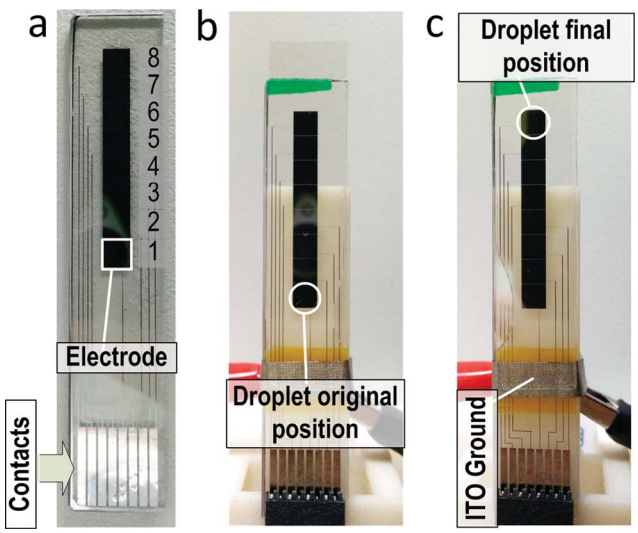

Fig. 7 (a) Fabricated DMF chip. For illustration, the electrodes are numbered 1–8; (b) and (c) operation of the DMF platform. The droplet was originally placed at electrode no. 1 (highlighted by the circle). By applying a signal on electrode no. 2 and then turning off electrode no. 1, the droplet moved to electrode no. 2. As such, the droplet can be transported to electrode no. 8, which is the NMR sensing site.

concentration of biotinylated iron nanoparticle should be well designed. Excessive amount of iron nanoparticles will diminish the echoes' amplitude rapidly (low T_2) and result in difficulty in acquiring the NMR signal. Detailed relationship between concentration of Iron nanoparticle and the limit of detection of avidin can be found elsewhere.[17]

The sample under assay was placed at electrode no. 1 and the probe (droplets with nanoparticles) was placed at electrode no. 8. These two droplets will combine together at electrode no. 7 to form a larger droplet, as shown in Fig. 8(a). To ensure the droplet mixed thoroughly, it was shuffled between electrode no. 6 and no. 8 several times. Then, the droplet was moved to electrode no. 8 for NMR sensing.

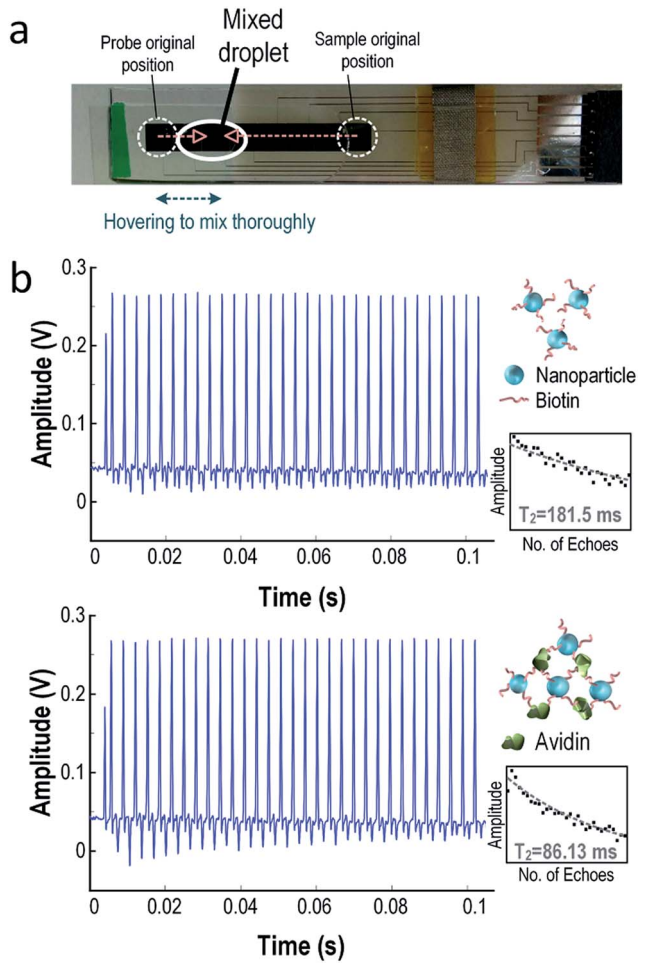

Fig. 8 (a) Illustration of droplets mixing. The droplets at electrode no. 1 (samples) and no. 8 (probe) were driven to electrode no. 7 and mixed together. (b) The NMR assay results from the mixed droplets. Biotinylated magnetic nanoparticles acted as a probe. If the samples do not contain avidin, the nanoparticles will stay monodispersed and a longer T_2 will be obtained (181.5 ms). If avidin is with the samples, avidin and biotin will combine to form a rigid bond, and clusters will be presented. Consequently, T_2 will be decreased by the perturbation of the magnetic nanoparticle clusters (86.13 ms). This shows that the system is capable of detecting the existence of protein in the samples in a fully-automated way.

Fig. 8(b) shows the received NMR signal with and without avidin. Without avidin in the sample (*i.e.* sample only contains water), T_2 of the droplets is 181.5 ms. When avidin presents in the target droplet, it will bind to the biotin and form a larger cluster. Consequently, T_2 of the droplets will be decreased to 86.13 ms with ΔT_2 of −52.55%. The error in T_2 of the NMR signals will decrease proportionally to the concentration of the targets in the samples, as suggested in previous research.[17] These results show that the NMR–DMF platform can successfully detect the existence of a specific target in the samples in a fully automatic manner. The results promise that this system is a low-cost NMR-based diagnostic tool with high portability and electronic automation.

5. Discussion

Interference from silicone oil

Surrounding the droplet samples by silicone oil is common in DMF to lower the required driving voltage and prevent sample vaporization. However, as silicone oil also contains hydrogen atoms, it will produce NMR signals, and their T_2 is comparable to water (oil: 314.5 ms), affecting the sensitivity. To prevent the interference from silicone oil, the figure-8 shaped coil should be designed such that the sensitive region is all covered by the droplets. The sensitive region is midway to the two coils (Fig. 9) that jointly generate an adequate plane-parallel magnetic flux. Outside the region, the magnetic flux is smaller than half of its peak value, making the NMR signal weak enough, and thus it can be neglected. As a consequence, the assay location of the sample should be well-monitored by the DMF chip under real-time feedback control[25] and has a surface area covering the sensitive region such that the silicone oil cannot affect the result, and the position error becomes more tolerable. Here, the sensitive region of a 14-turn figure-8 shaped coil has a diameter of 4.2 mm, which is fully covered by the droplet having a diameter of 6.3 mm.

Potential applications

Unlike the spiral coil, the figure-8 shaped coil is capable of generating a plane-parallel RF-field, making it a powerful tool to

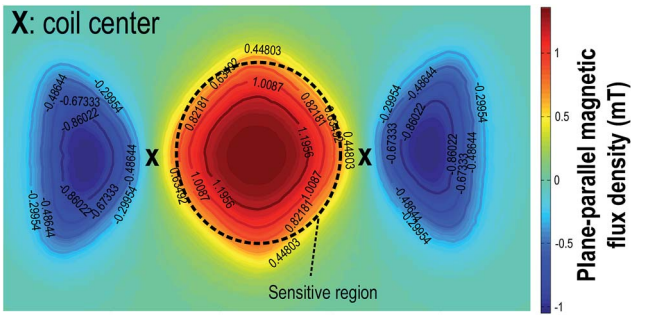

Fig. 9 Plane-parallel magnetic flux density map of the 14-turn figure-8 shaped coil at $z = 0.6$ mm (depth of the ITO glass). The sensing region, which is defined as the area, has a plane-parallel magnetic flux density larger than 50%; its peak value (1.43 mT) is located between the centers of two coils and has a shape of a circle with diameter around 4.2 mm.

be integrated with the planar DMF chip. A wide variety of applications can be considered over the NMR–DMF system. Simultaneous detection of multiple biomarkers in a sample is crucial in bio-assays.[43] This system can perform NMR sensing on different sites simultaneously with multiple figure-8 shaped coils since the space available inside the magnet is enlarged. This can deliver a higher throughput which is suitable for drug screening.

Other potential applications include cell incubation and detection in DMF platform, which is getting more attractive in recent years.[24,44–51] With the confirmation that DMF has a negligible effect on the vitality and characteristics of the cells,[24,52] it is favorable for operation with mass-limited cell samples. Typical cell characteristic assays on DMF include absorbance test,[23] fluorescence,[24,49] surface plasmon resonance[53] and impedance sensing.[54] These methods either require bench-top equipment (fluorescence, surface plasmon resonance), which have limited sensitivity (absorbance test) or are non-specific (impedance sensing). On the other hand, NMR could be more promising for cell targeting and quantitative analysis, including cancer cells for early cancer diagnosis, and it can provide high sensitivity assays.[17,19,55–57] Yet, before NMR operation, a series of manual preparation (*e.g.*, cell culturing) has to be performed. With the described NMR–DMF system, NMR assays can be performed with minimal human operations. DMF platform may include a culturing site for cell culturing within DMF.[46,48] Thus, all operations could be well-guided by the computer.

Similarly, deoxyribonucleic acid (DNA) can also be amplified on the DMF platform,[58–60] which can reduce the operation time and samples' consumption when compared with bench-top PCR machines. However, the detection method of those on-chip PCR machines mainly relies on general gel electrophoresis, which could not be integrated with the DMF platform. On the other hand, NMR assays are able to perform sensitive DNA/oligonucleotide targeting,[15,61–63] including practical applications such as detection of pathogens,[18] bacteria[64] and fungus in the whole blood.[65] With the NMR–DMF system, the human operation is greatly simplified. The DNA amplification and targeting in NMR can be performed inside the chip without human effort such that the detection time and chance of contamination are minimized.

6. Conclusions

In summary, a modular integration of NMR and DMF has been demonstrated. We overcome the geometrical limitations among the traditional spiral coil, planar DMF chip and portable magnet by introducing a figure-8 shaped coil, which could be fabricated with low-cost PCB with high reproducibility. Extensive studies and experiments verified the compatibility and co-functionality of the two distinctive technologies: NMR (assay tool) and DMF (droplet sample operation). The electronic-automated real-time identification of avidin/biotinylated magnetic nanoparticle pairs proved the biological assay capability of the system. Compared to the micro-channel NMR, this system improves droplet management, allowing multi-step screening protocols guided by simple electronics. Potential applications such as DNA amplification and detection were also discussed, showing the prospects of extending such a NMR–DMF system to different biological applications.

Acknowledgements

The authors gratefully acknowledge J. Gao for fabricating the DMF chips, T. Chen for assisting the setup of the DMF actuator and Y. Jia for technical review. This work was funded by the University of Macau and Macau Science and Technology Development Fund (FDCT) under the project (033/2011/A2) and the State Key Lab fund.

Notes and references

1 G. J. Kost, *Principles and Practice of Point-of-Care Testing*, Lippincott Williams & Wilkins, Philadelphia, 2002.
2 M. Urdea, L. A. Penny, S. S. Olmsted, M. Y. Giovanni, P. Kaspar, A. Shepherd, P. Wilson, C. A. Dahl, S. Buchsbaum, G. Moeller and D. C. H. Burgess, *Nature*, 2006, **444**, 73–79.
3 C. D. Chin, V. Linder and S. K. Sia, *Lab Chip*, 2007, **7**, 41–57.
4 P. Yager, G. J. Domingo and J. Gerdes, *Annu. Rev. Biomed. Eng.*, 2008, **10**, 107–144.
5 D. A. Giljohann and C. A. Mirkin, *Nature*, 2009, **462**, 461–464.
6 C. P. Price, A. St John and L. J. Kricka, *Point-of-care testing*, AACC Press, Washington DC, 3rd edn, 2010.
7 D. G. Storla, S. Yimer and G. A. Bjune, *BMC Public Health*, 2008, **8**, 15–23.
8 A. Balasubramanian, B. Bhuva, R. Mernaugh and F. R. Haselton, *IEEE Sens. J.*, 2005, **5**(3), 340–344.
9 C. Stagni, C. Guiducci, L. Benini, B. Riccò, S. Carrara, C. Paulus, M. Schienle and R. Thewes, *IEEE Sens. J.*, 2007, **7**(4), 577–585.
10 S. Emaminejad, M. Javanmard, R. W. Dutton and R. W. Davis, *Lab Chip*, 2012, **12**, 4499–4507.
11 T. Aytur, J. Foley, M. Anwar, B. Boser, E. Harris and P. R. Beatty, *J. Immunol. Methods*, 2006, **314**(1–2), 21–29.
12 P. Liu, K. Skucha, M. Megens and B. Boser, *IEEE Trans. Magn.*, 2011, **47**(10), 3449–3451.
13 M. L. Simpson, G. S. Sayler, G. Patterson, D. E. Nivens, E. K. Bolton, J. M. Rochelle, J. C. Arnott, B. M. Applegate, S. Ripp and M. A. Guillorn, *Sens. Actuators, B*, 2001, **72**(2), 134–140.
14 H. Eltoukhy, K. Salama and A. E. Gamal, *IEEE J. Solid-State Circuits*, 2006, **41**(3), 651–662.
15 L. Josephson, J. M. Perez and R. Weissleder, *Angew. Chem., Int. Ed.*, 2001, **113**(17), 3304–3306.
16 J. M. Perez, L. Josephson, T. O'Loughlin, D. Högemann and R. Weisselder, *Nat. Biotechnol.*, 2002, **20**, 816–820.
17 H. Lee, E. Sun, D. Ham and R. Weissleder, *Nat. Med.*, 2008, **14**(8), 869–874.
18 M. Liong, A. N. Hoang, J. Chung, N. Gural, C. B. Ford, C. Min, R. R. Shah, R. Ahmad, M. Fernandez-Suarez, S. M. Fortune, M. Toner, H. Lee and R. Weissleder, *Nat. Commun.*, 2013, **4**(1752), 1–9.

19 N. Sun, T.-J. Yoon, H. Lee, W. Andress, R. Weissleder and D. Ham, *IEEE J. Solid-State Circuits*, 2011, **46**(1), 342–352.
20 J. D. Trumbull, I. K. Glasgow, D. J. Beebe and R. L. Magin, *IEEE Trans. Biomed. Eng.*, 2000, **47**(1), 3–7.
21 C. Massin, F. Vincent, A. Homsy, K. Ehrmann, G. Boero, P.-A. Besse, A. Daridon, E. Verpoorte, N. F. de Rooij and R. S. Popovica, *J. Magn. Reson.*, 2003, **164**(2), 242–255.
22 M. G. Pollack, A. D. Shenderov and R. B. Fair, *Lab Chip*, 2002, **2**, 96–101.
23 V. Srinivasan, V. K. Pamula and R. B. Fair, *Lab Chip*, 2004, **4**, 310–315.
24 I. Barbulovic-Nad, H. Yang, P. S. Park and A. R. Wheeler, *Lab Chip*, 2008, **8**, 519–526.
25 J. Gao, X. Liu, T. Chen, P. I. Mak, Y. Du, M.-I. Vai, B. Lin and R. P. Martins, *Lab Chip*, 2013, **13**, 443–451.
26 M. H. Shamsi, K. Choi, A. H. C. Ng and A. R. Wheeler, *Lab Chip*, 2014, **14**, 547–554.
27 N. E. Jacobsen, *NMR Spectroscopy Explained*, John Wiley & Sons, Hoboken, 2007.
28 D. I. Hoult and R. E. Richards, *J. Magn. Reson.*, 1976, **24**, 71–85.
29 J. Kim, B. Hammer and R. Harjani, *IEEE Custom Integrated Circuits Conference*, San Jose, 2012, pp. 1–4.
30 J. Anders, P. SanGiorgio and G. Boreo, *J. Magn. Reson.*, 2011, **209**(1), 1–7.
31 J. Perlo, V. Demas, F. Casanova, C. A. Meriles, J. Reimer, A. Pines and B. Blümich, *Science*, 2005, **308**(5726), 1279.
32 B. Blümich, V. Anferov, S. Anferova, M. Klein, R. Fechete, M. Adams and F. Casanova, *Concepts Magn. Reson.*, 2002, **15**(4), 255–261.
33 N. M. Neihart, D. J. Allstot, M. Miller and P. Rakers, *IEEE 2008 Custom Integrated Circuits Conference*, San Jose, 2008, pp. 575–578.
34 J. Einzinger and A. Loth, *US Pat.*, no. 7,642,891, 2010.
35 M. Nagata, H. Masuoka, S.-I. Fukase, M. Kikuta, M. Morita and N. Itoh, *IEEE Bipolar/BiCMOS Circuits Technol. Meet.*, Maastricht, 2006, pp. 1–4.
36 T. Mattsson, *US Pat.*, no. 7,151,430, 2006.
37 P. Andreani, K. Kozmin, P. Sandrup, M. Nilsson and T. Mattsson, *IEEE J. Solid-State Circuits*, 2011, **46**(7), 1618–1626.
38 F. Fiorillo and C. Beatrice, *J. Supercond. Novel Magn.*, 2011, **24**, 559–566.
39 J. M. Pope and N. Repin, *Magn. Reson. Imaging*, 1988, **6**, 641–646.
40 W. K. Peng, L. Chen and J. Han, *Rev. Sci. Instrum.*, 2012, **83**, 095115.
41 B. Blümich, J. Perlo and F. Casanova, *Prog. Nucl. Magn. Reson. Spectrosc.*, 2008, **52**, 197–269.
42 F. Casanova, J. Perlo and B. Blümich, *Single-sided NMR*, Springer, Germany, 2011.
43 M. Muluneh and D. Issadore, *Adv. Drug Delivery Rev.*, 2013, **66**, 101–109.
44 S. K. Fan, P. W. Huang, T. T. Wang and Y. H. Peng, *Lab Chip*, 2008, **8**, 1325–1331.
45 G. J. Shah, A. T. Ohta, E. P.-Y. Chiou, M. C. Wu and C. J. Kim, *Lab Chip*, 2009, **9**, 1732–1739.
46 I. Barbulovic-Nad, S. H. Au and A. R. Wheeler, *Lab Chip*, 2010, **10**, 1536–1542.
47 D. Witters, N. Vergauwe, S. Vermeir, F. Ceyssens, S. Liekens, R. Puers and J. Lammertyn, *Lab Chip*, 2011, **11**, 2790–2794.
48 S. Srigunapalan, I. A. Eydelnant, C. A. Simmons and A. R. Wheeler, *Lab Chip*, 2012, **12**, 369–375.
49 D. Bogojevic, M. D. Chamberlain, I. Barbulovic-Nad and A. R. Wheeler, *Lab Chip*, 2012, **12**, 627–634.
50 V. Chokkalingam, J. Tel, F. Wimmers, X. Liu, S. Semenov, J. Thiele, C. G. Figdor and W. T. S. Huck, *Lab Chip*, 2013, **13**, 4740–4744.
51 G. S. Du, J. Z. Pan, S. P. Zhao, Y. Zhu, J. M. J. den Toonder and Q. Fang, *Anal. Chem.*, 2013, **85**(14), 6740–6747.
52 S. H. Au, R. Fobel, S. P. Desai, J. Voldman and A. R. Wheeler, *Integr. Biol.*, 2013, **5**, 1014–1025.
53 L. Malic, T. Veres and M. Tabrizian, *Lab Chip*, 2009, **9**, 473–475.
54 S. C. C. Shih, I. Barbulovic-Nad, X. Yang, R. Fobel and A. R. Wheeler, *Biosens. Bioelectron.*, 2013, **42**, 314–320.
55 I. J. M. de Vries, W. J. Lesterhuis, J. O. Barentsz, P. Verdijk, J. H. van Krieken, O. C. Boerman, W. J. G. Oyen, J. J. Bonenkamp, J. B. Boezeman, G. J. Adema, J. W. M. Bulte, T. W. J. Scheenen, C. J. A. Punt, A. Heerschap and C. G. Figdor, *Nat. Biotechnol.*, 2005, **23**(11), 1407–1413.
56 J. B. Haun, N. K. Devaraj, S. A. Hilderbrand, H. Lee and R. Weissleder, *Nat. Nanotechnol.*, 2010, **5**(9), 660–665.
57 A. V. Ullal, T. Reiner, K. S. Yang, R. Gorbatov, C. Min, D. Issadore, H. Lee and R. Weissleder, *ACS Nano*, 2011, **5**(11), 9216–9224.
58 Y. H. Chang, G. B. Lee, F. C. Huang, Y. Y. Chen and J. L. Lin, *Biomed. Microdevices*, 2006, **8**, 215–225.
59 R. Sista, Z. Hua, P. Thwar, A. Sudarsan, V. Srinivasan, A. Eckhardt, M. Pollack and V. Pamula, *Lab Chip*, 2008, **8**, 2091–2104.
60 Z. Hua, J. L. Rouse, A. E. Eckhardt, V. Srinivasan, V. K. Pamula, W. A. Schell, J. L. Benton, T. G. Mitchell and M. G. Pollack, *Anal. Chem.*, 2010, **82**(6), 2310–2316.
61 J. Grimm, J. M. Perez, L. Josephson and R. Weissleder, *Cancer Res.*, 2004, **64**(2), 639–643.
62 C. Min, H. Shao, M. Liong, T. J. Yoon, R. Weissleder and H. Lee, *ACS Nano*, 2012, **6**(8), 6821–6828.
63 W. Ma, H. Yin, L. Xu, L. Wang, H. Kuang and C. Xu, *Chem. Commun.*, 2013, **49**, 5369–5371.
64 H. J. Chung, C. M. Castro, H. Im, H. Lee and R. Weissleder, *Nat. Nanotechnol.*, 2013, **8**, 369–375.
65 L. A. Neely, M. Audeh, N. A. Phung, M. Min, A. Suchocki, D. Plourde, M. Blanco, V. Demas, L. R. Skewis, T. Anagnostou, J. J. Coleman, P. Wellman, E. Mylonakis and T. J. Lowery, *Sci. Transl. Med.*, 2013, **5**(182), 182ra54.